Nano Energy 144 (2025) 111339

Contents lists available at ScienceDirect

Nano Energy

journal homepage: www.elsevier.com/locate/nanoen

Vortex-flutter internal resonance: A new mechanism for wind energy harvesting

Liwei Dong [a], Qian Tang [b], Xin Li [c], Chaoyang Zhao [a], Chengjia Han [a], Guobiao Hu [d], Fan Yang [e,f,*], Yaowen Yang [a,**]

[a] School of Civil and Environmental Engineering, Nanyang Technological University, 50 Nanyang Avenue, Singapore 639798, Singapore
[b] School of Physics and New Energy, Chongqing University of Technology, Chongqing 400054, China
[c] Guanzhou Institute of Technology, Xidian University, Guangzhou, Guangdong 510555, China
[d] Internet of Things Thrust, The Hong Kong University of Science and Technology (Guangzhou), Nansha, Guangzhou, Guangdong 511400, China
[e] Department of Orthopaedics, Shanghai Key Laboratory for Prevention and Treatment of Bone and Joint Diseases, Shanghai Institute of Traumatology and Orthopaedics, Ruijin Hospital, Shanghai Jiao Tong University School of Medicine, Shanghai 200025, China
[f] Research Institute of Frontier Science, Southwest Jiaotong University, Chengdu, Sichuan 610031, China

ARTICLE INFO

Keywords:
Wind energy harvesting
Flow-induced vibration
Vortex-induced vibration
Flutter
Wireless sensor node

ABSTRACT

Flow-induced vibrations (FIVs), traditionally regarded as structural hazards, offer significant untapped potential for ambient wind energy harvesting. Here, we report the first experimental implementation and theoretical investigation of internal resonance arising from the coupling between vortex-induced vibration (VIV) and flutter, which enables a new class of high-performance wind energy harvesters (WEHs). This coupling produces a synergistic interaction where the flutter-induced aerodynamic instability facilitates a 25-fold increase in power output at the critical onset, and the internal resonance mode outperforms VIV alone by a factor of 5. To explain this behavior, we develop an aero-electro-mechanical model that captures the emergence and characteristics of the internal resonance. Further experiments show that this internal resonance can be precisely tuned by adjusting the flag position and geometry, offering flexible and application-specific WEH design. Finally, we demonstrate the practical utility of the vortex-flutter coupled WEH by powering a wireless sensor node for real-time temperature monitoring. This work opens promising new pathways for aerodynamic WEHs by leveraging strong intermodal coupling between FIV mechanisms.

1. Introduction

Wind is a widely available and renewable energy source found across diverse natural and built environments. With continuous advancements in energy harvesting technologies, wind energy harvesting has attracted sustained scientific attention since the late 19th century. This has led to the emergence of various wind energy harvesters (WEHs) based on triboelectric [1–3], piezoelectric [4–6], and electromagnetic [7–9] mechanisms, tailored to specific power demands and application scales. Recently, research has increasingly focused on microscale WEHs [10], where harvested wind energy offers a practical solution for powering wireless sensor networks (WSNs). These battery-free, self-sustaining systems are expected to accelerate the deployment of Internet of Things (IoT) technologies [11], enabling autonomous and sustainable operation in both urban and remote areas.

WEHs can be broadly categorized into two categories based on their operational principles: rotary and flow-induced vibration (FIV) systems [12]. Rotary WEHs, such as those utilizing wind cups or turbines, generate electricity through rotational motion and various energy conversion mechanisms [13–15]. However, these systems are typically bulky and exhibit limited efficiency at low wind speeds due to rotor inertia and startup resistance [16]. FIV-based WEHs harness energy through fluid-structure interactions that induce mechanical vibrations in structures such as beams [17], cylinders [18], or membranes [19]. These vibrations, manifesting as vortex-induced vibration (VIV) [20,21], galloping [22], flutter [23,24], or wake galloping [25], are

* Corresponding author at: Department of Orthopaedics, Shanghai Key Laboratory for Prevention and Treatment of Bone and Joint Diseases, Shanghai Institute of Traumatology and Orthopaedics, Ruijin Hospital, Shanghai Jiao Tong University School of Medicine, Shanghai 200025, China.
** Corresponding author.
E-mail addresses: yf12498@sjtu.edu.cn (F. Yang), cywyang@ntu.edu.sg (Y. Yang).

https://doi.org/10.1016/j.nanoen.2025.111339
Received 20 June 2025; Received in revised form 15 July 2025; Accepted 21 July 2025
Available online 22 July 2025

subsequently converted into electrical energy. FIV-based WEHs offer notable advantages, including compact form factors and high performance in low wind conditions [26], making them well-suited for powering remote WSNs in urban environments.

Despite their advantages, FIV-based WEHs face challenges in delivering sufficient electrical output due to the broadband and unsteady excitation, which arises from fluctuating aerodynamic forces. To address these limitations, various strategies have been explored, including multi-degree-of-freedom architectures [27–29], multi-stable configurations [30–32], the incorporation of base excitations [33–35], and the combination of multiple FIV modes [36–38]. The first two approaches aim to broaden the operational bandwidth by leveraging structural complexity and introducing nonlinear restoring forces. The incorporation of base excitations can significantly enhance performance when an internal resonance between the excitation and FIV is activated; however, this approach requires precise parameter tuning and increases design complexity. Coupling multiple FIV modes often involves customizing bluff body geometries to facilitate transitions between vibration modes across varying flow regimes [32,33]. Another strategy integrates WEHs based on distinct FIV mechanisms to achieve additive performance [38]. While such combinations enhance operational robustness under variable wind speeds, they do not fundamentally improve energy harvesting efficiency or power density.

The coupling and interaction of multiple FIV modes remain largely unexplored, primarily due to their distinct dynamic characteristics, which often hinder synergistic effects and may even result in mutual suppression. In this study, we report the first observation and investigation of an internal resonance caused by VIV-flutter coupling (referred to as vortex-induced internal resonance hereafter), offering a novel perspective for enhancing wind energy harvesting. By incorporating a flexible flag into a classic VIV-based WEH, flutter forces are introduced, enabling vortex-flutter internal resonance through simple geometric tuning of the flag. This coupling can lead to a marked improvement in wind energy conversion efficiency. To elucidate the underlying mechanism, we develop an aerodynamic model that integrates beam segment dynamics, piezoelectric coupling, and both VIV and flutter effects. The model successfully captures the coupling behavior and is validated through wind tunnel experiments. We further compare the time-frequency responses and power outputs of the vortex-flutter coupled WEH (VFC-WEH) with those of a traditional VIV-based WEH, followed by a series of experimental investigations under various flutter configurations. Finally, we demonstrate the practical potential of the proposed VFC-WEH by powering a WSN for mobile temperature monitoring.

2. Results

2.1. Principle of VFC-WEH

The concept of vortex-flutter internal resonance is inspired by magnetically-coupled inductive wireless power transfer (MCI-WPT) technology [39]. As illustrated in Fig. 1a, unlike conventional inductive wireless power transfer (IWPT) systems that rely on a single resonant circuit, MCI-WPT utilizes a pair of resonant circuits to achieve magnetic resonance coupling when the transmitting and receiving coil frequencies align. This magnetic resonance significantly enhances both power transfer efficiency and transmission distance. Drawing inspiration from this synergistic mechanism, a novel vortex-flutter coupling is proposed for wind energy harvesting. In this configuration, a cylindrical bluff body induces VIV, while a flexible flag yields flutter excitations (Fig. 1c). The interactions of the bluff body and the flag with the surrounding airflow can be respectively represented as VIV and flutter mass-spring-damper subsystems, analogous to the paired resonant circuits in the MCI-WPT. To enhance wind energy harvesting performance, these two FIV modes are expected to achieve strong coupling through careful design.

The VFC-WEH is readily implemented by integrating a flexible flag into a classic VIV-based WEH (Fig. 1c). While the VIV frequency remains relatively constant closely aligned with the structural natural frequency, the flutter frequency increases with wind speed. This enables the internal resonance to be both tunable and designable by adjusting the geometric dimensions of the flag. When the flutter frequency of the flag matches the VIV frequency induced by the bluff body, internal resonance is activated in the aluminum beam. The use of a macro fiber composite (MFC) attached near the fixed end of the beam ensures efficient transduction of mechanical strain into piezoelectrical output under the internal resonance, thereby achieving effective wind energy conversion. Compared to recently reported VIV-based WEHs [31,38,40–43], the proposed VFC-WEH demonstrates superior power performance, highlighting its improved practicality for harvesting breeze energy (Fig. 1b).

To optimize energy harvesting in real-world environments, the flag geometry and position must be carefully designed to achieve frequency matching and effectively regulate flutter-induced torque (Fig. 1d). This flexible and high-performance harvester can be deployed in environments such as roadsides, where it simultaneously captures ambient wind and vehicle-induced airflow. The harvested energy can support the continuous operation of GPS modules, temperature and humidity sensors, and speed detectors, thereby enabling energy self-sufficiency of distributed WSNs.

2.2. Theoretical modeling

To elucidate the vortex-flutter coupling mechanism and inform the activation of internal resonance, we develop an aero-electro-mechanical model that integrates beam segment dynamics, piezoelectric coupling, and both VIV and flutter effects. Due to the complex nature of flag flutter and the inherent challenges in fully capturing fluid–structure interactions, the flutter force is approximated as an external periodic excitation acting on the VIV system. The dynamics of the coupled system (upper inset of Fig. 2a) are governed by the Euler-Bernoulli beam equation

$$E_cI_c\frac{\partial^4 w(x,t)}{\partial x^4}+C_a\frac{\partial w(x,t)}{\partial t}+C_sI_c\frac{\partial^5 w(x,t)}{\partial x^4\partial t}+m\frac{\partial^2 w(x,t)}{\partial t^2}+F_{viv\_damping}\delta(x-L)$$
$$+\theta_p V(t)\left[\frac{d\delta(x-L_2)}{dx}-\frac{d\delta(x-L_1)}{dx}\right]=F_{viv}\delta(x-L)+F_{flutter} \tag{1}$$

where E_cI_c denotes the equivalent bending stiffness of the composite beam; L is the beam length; and $w(x, t)$ refers to the displacement with the position x and time t. C_a and C_s denote represent the strain-related and viscous air damping coefficients, respectively, while m is the distributed mass of the composite beam.

The VIV contribution includes a fluid-added damping force acting on the bluff body $F_{damping}$ and a vortices-induced aerodynamic force F_{viv}, given by [44]

$$\begin{cases} F_{viv\_damping}=\dfrac{1}{2}C_d\rho_a HDU\dfrac{dw(L,t)}{dt} \\ F_{viv}=\dfrac{1}{4}C_{l0}\rho_a HDU^2 q(t) \end{cases} \tag{2}$$

where C_d and C_{l0} denote the mean drag coefficient and steady lift coefficient of the bluff body, respectively; ρ_a represents the air density; H and D refer to the height and diameter of the bluff body; U is the wind speed; and q is a dimensionless wake variable used to characterize the fluctuating behavior of the vortex-induced lift coefficient, and modeled by a wake oscillator governed by the van der Pol equation [45]

$$\begin{cases} \ddot{q}(t)+\varepsilon\omega_f\left[q^2(t)-1\right]\dot{q}(t)+{\omega_f}^2 q(t)=F_q \\ F_q=\dfrac{A}{D}\dfrac{d^2w_3(L,t)}{dt^2} \end{cases} \tag{3}$$

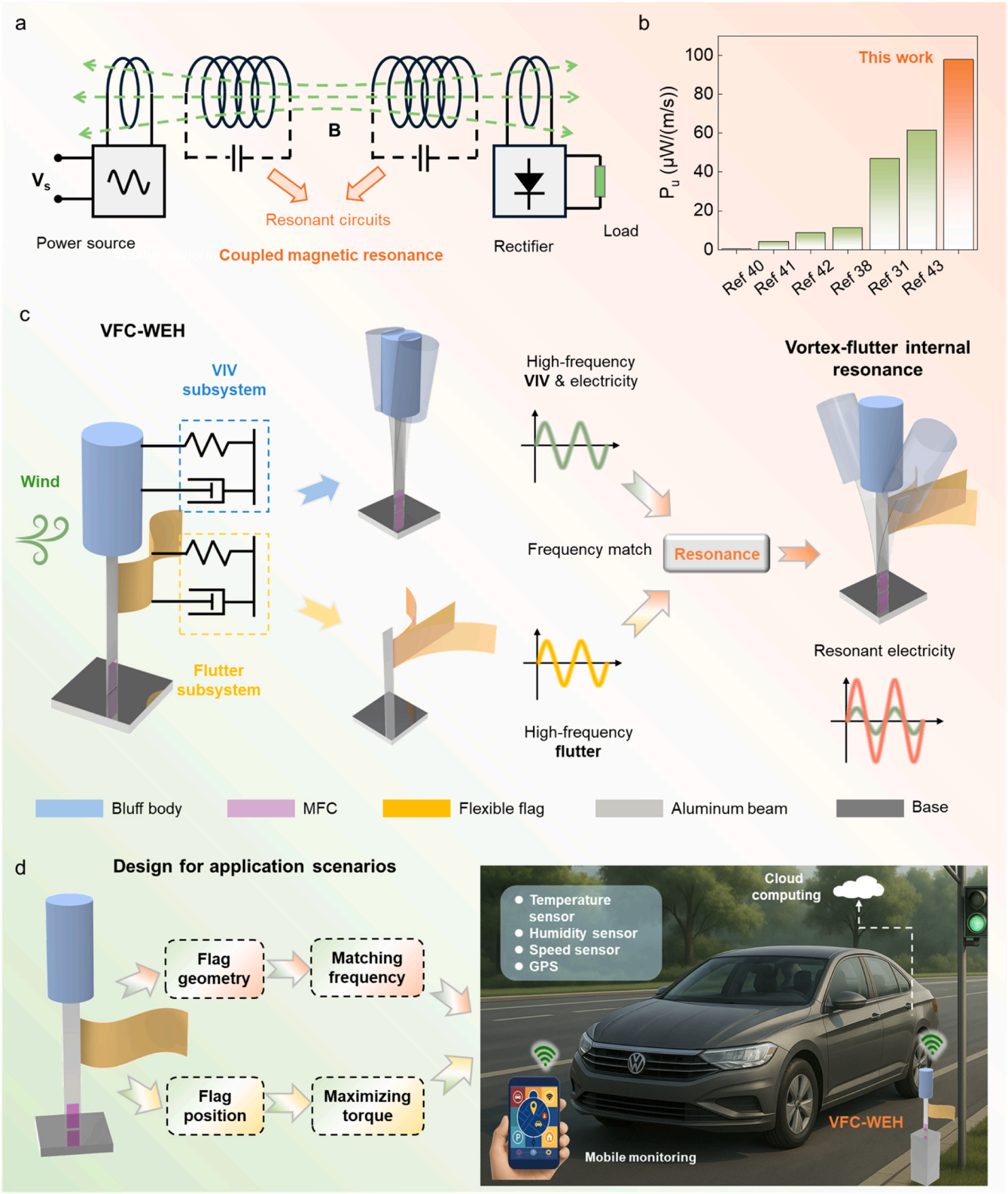

Fig. 1. Principle and wind energy harvesting application of vortex-flutter internal resonance. (a) Illustration of vortex-flutter internal resonance inspired by the MCI-WPT technology. (b) Comparison of VFC-WEH with other advanced VIV-based WEHs. (c) Configuration and principle of VFC-WEH. The VFC-WEH can be implemented through the introduced of a flexible flag in a classic VIV-based WEH. When the flag flutter frequency matches the VIV frequency induced by the bluff body, vortex-flutter internal resonance can be triggered, thus enhancing the wind energy harvesting performance. (d) Harvester design for real-world self-powered application scenarios.

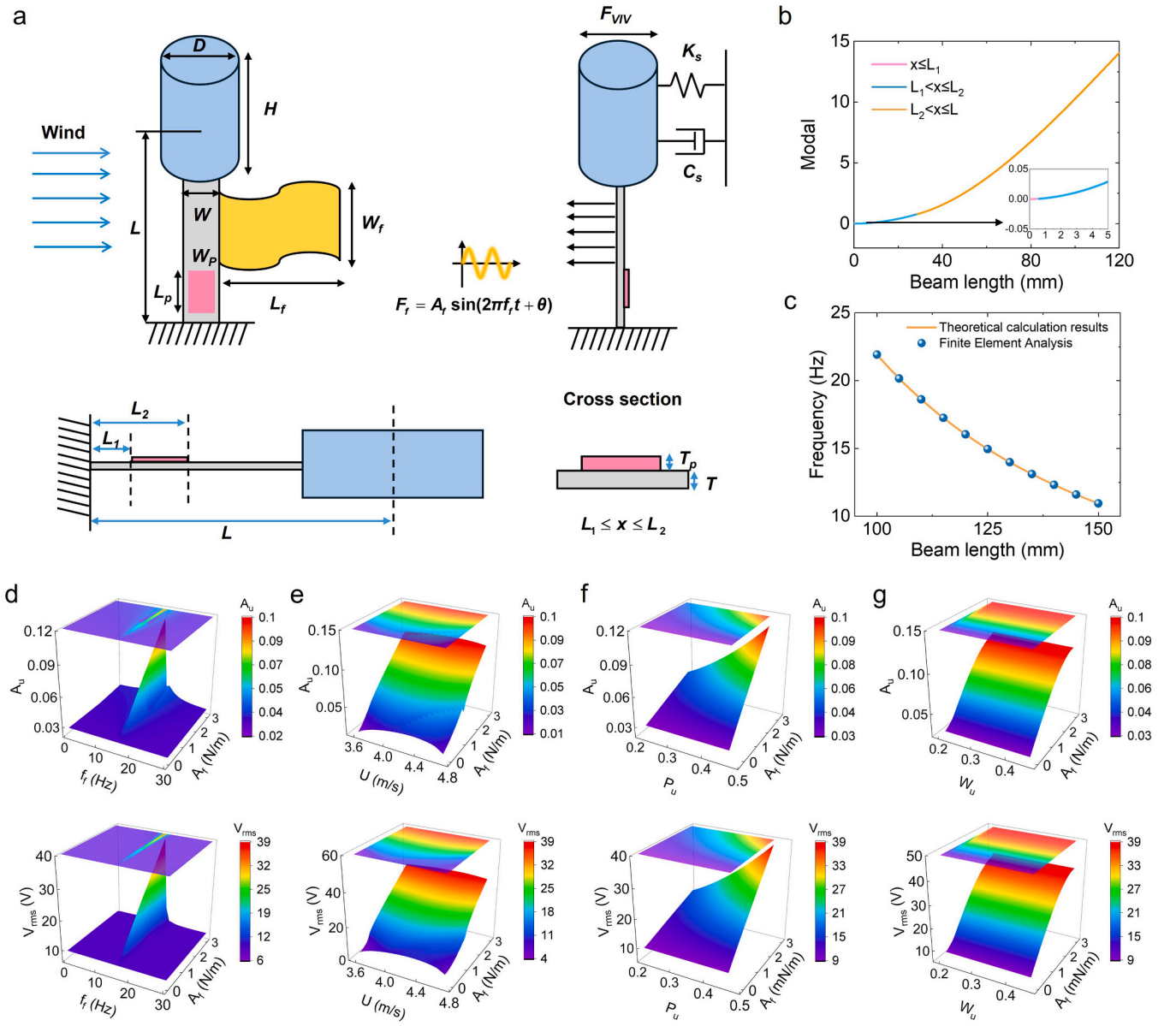

Fig. 2. Theoretical modeling and analysis of vortex-flutter coupling. (a) Aerodynamic model of VFC-WEH considering the beam segmentation dynamics, piezoelectric coupling effect, VIV and flutter forces. (b) First mode shape of the beam calculated by the developed model. (c) Validation of natural frequency results calculated by the model through finite element simulations. (d) Coupled vibration amplitude and RMS voltage versus flutter force amplitude and frequency with U= 4 m/s, P_u= 0.45, and W_u= 0.42. (e) Coupled vibration amplitude and RMS voltage versus flutter force amplitude and frequency with f_f= 16 Hz, P_u= 0.45, and W_u= 0.42. (f) Coupled vibration amplitude and RMS voltage versus flag position and flutter force amplitude with U= 4 m/s, f_f= 16 Hz, and W_u= 0.42. (g) Coupled vibration amplitude and RMS voltage versus flag width and flutter force amplitude with U= 4 m/s, f_f= 16 Hz, and P_u= 0.45.

where $\omega_f = 2\pi S_t U/D$ refers to the vortex shedding frequency, with S_t being the Strouhal number.

The flutter-induced force from the flag is transmitted to the aluminum beam through its fixed end and is modeled as a discretely applied periodic line load with amplitude A_f, frequency f_f, and phase θ along the beam

$$F_{flutter} = \sum_{j=1}^{n+1} A_f \sin\left(2\pi f_f t + \theta\right)\delta\left[x - P_f + \frac{W_f}{2} + \frac{W_f}{n}\left(j-1\right)\right] \tag{4}$$

where P_f denotes the flag center position; W_f is the flag width; and n denotes the discrete interval along the beam.

The electromechanical coupling effect induced by the MFC is described by [33]

$$C_p \dot{V}_p(t) + I_p(t) - \theta_p \int_{L_1}^{L_2} \frac{\dot{w}(x,t)}{\partial x^2 \partial t} dx = 0 \tag{5}$$

where C_p refers to the internal capacitance of MFC; and V_p and I_p are voltage and current across the external circuit. The electromechanical coupling coefficient is given by $\theta_p = -E_p d_{31} W_p h_{pc}$, with E_p, d_{31}, W_p, and h_{pc} being the Young's modulus, the piezoelectric constant, the width of the MFC sheet, and the center of the MFC to the neutral axis. L_1 and L_2 represent the positions of MFC's both ends along the beam.

Since the MFC does not fully cover the host beam (below inset of Fig. 2a), segment modeling approach is required to accurately capture the system's dynamic behavior. Accordingly, the bending stiffness and mass terms in Eq. (1) are expressed as [46]

$$\begin{cases} EI_1 = EWT^3/12,\ 0 \le x < L_1 \\ EI_2 = EW\left(T_b^3 - T_a^3\right)/3 + E_pW_p\left(T_c^3 - T_b^3\right)/3,\ L_1 \le x < L_2 \\ EI_3 = EWT^3/12,\ L_2 \le x < L \end{cases} \tag{6}$$

$$\begin{cases} m_1 = \rho TW,\ 0 \le x < L_1 \\ m_2 = \rho TW + \rho_p T_p W_p,\ L_1 \le x < L_2 \\ m_3 = \rho TW,\ L_2 \le x < L \end{cases} \tag{7}$$

where E, ρ, W and T denote the Young's modulus, density, width and thickness of the host beam, respectively; ρ_p and T_p are the density and thickness of the MFC; and T_a, T_b, and T_c represent the distances from the neutral axis to the bottom of the host beam, the bottom and the top of the MFC, respectively.

The natural frequencies and mode shapes of the composite beam are obtained using Euler-Bernoulli beam theory [47]. The analysis begins with the case of undamped free vibration in the absence of aerodynamic forces. In this scenario, each beam segment is governed by

$$EI_i\frac{\partial^4 w_i(x_i,t)}{\partial x_i^4} + m_i(x_i)\frac{\partial^2 w_i(x_i,t)}{\partial t^2} = 0 \tag{8}$$

where $i = 1,2$ and 3 denotes the three beam segments, corresponding to $0 < x_1 < L_1$, $L_1 < x_2 < L_2$, $L_2 < x_3 < L$, respectively. The boundaries at $x_1 = 0$ and $x_3 = L$ are specified as

$$\begin{cases} w_1(x_1,t)|_{x_1=0} = 0 \\ \dfrac{w_1(x_1,t)}{\partial x_1}|_{x_1=0} = 0 \end{cases} \tag{9}$$

$$\begin{cases} EI_3\dfrac{\partial^3 w_3(x_3,t)}{\partial x_3^3}|_{x_3=L} = M_b\dfrac{\partial^2 w_3(x_3,t)}{\partial t^2}|_{x_3=L} \\ EI_3\dfrac{\partial^2 w_3(x_3,t)}{\partial x_3^2}|_{x_3=L} = -I_b\dfrac{\partial^3 w_3(x_3,t)}{\partial x_3\partial t^2}|_{x_3=L} \end{cases} \tag{10}$$

where M_b and I_b denote the mass and rotary inertia of the bluff body, respectively

The continuity transition at $x_1 = L_1$ and $x_2 = L_2$ are given as

$$\begin{cases} w_1(x_1,t)|_{x_1=L_1} = w_2(x_2,t)|_{x_2=L_1} \\ \dfrac{\partial w_1(x_1,t)}{\partial x_1}|_{x_1=L_1} = \dfrac{\partial w_2(x_2,t)}{\partial x_2}|_{x_2=L_1} \end{cases} \tag{11}$$

$$\begin{cases} EI_1\dfrac{\partial^2 w_1(x_1,t)}{\partial x_1^2}|_{x_1=L_1} = EI_2\dfrac{\partial^2 w_2(x_2,t)}{\partial x_2^2}|_{x_2=L_1} \\ EI_1\dfrac{\partial^3 w_1(x_1,t)}{\partial x_1^3}|_{x_1=L_1} = EI_2\dfrac{\partial^3 w_2(x_2,t)}{\partial x_2^3}|_{x_2=L_1} \end{cases} \tag{12}$$

$$\begin{cases} w_2(x_2,t)|_{x_2=L_2} = w_3(x_3,t)|_{x_3=L_2} \\ \dfrac{\partial w_2(x_2,t)}{\partial x_2}|_{x_2=L_2} = \dfrac{\partial w_3(x_3,t)}{\partial x_3}|_{x_3=L_2} \end{cases} \tag{13}$$

$$\begin{cases} EI_2\dfrac{\partial^2 w_2(x_2,t)}{\partial x_2^2}|_{x_2=L_2} = EI_3\dfrac{\partial^2 w_3(x_3,t)}{\partial x_3^2}|_{x_3=L_2} \\ EI_2\dfrac{\partial^3 w_2(x_2,t)}{\partial x_2^3}|_{x_2=L_2} = EI_3\dfrac{\partial^3 w_3(x_3,t)}{\partial x_3^3}|_{x_3=L_2} \end{cases} \tag{14}$$

The mode shapes for three segments of the beam can be expressed as

$$\varphi_{ir}(x) = A_{ir}\sin\beta_{ir}x + B_{ir}\cos\beta_{ir}x + C_{ir}\sinh\beta_{ir}x + D_{ir}\cosh\beta_{ir}x,\ i = 1,2,3 \tag{15}$$

where $\beta_{ir}^4 = {\omega_r}^2 m_i/EI_i$, and r represents the rth mode. By substituting the mode shape expression Eq. (15) into the boundary and continuity constraints (Eqs. (8)-(14)), an eigenvalue problem is formulated, resulting in a 12×12 coefficient matrix. By setting the determinant of this matrix to zero, the natural frequencies can be determined. Once the natural frequency is obtained, the corresponding mode shapes are derived by substituting it back into the coefficient matrix. Finally, a mass normalization procedure is applied to the mode shapes to ensure orthogonality.

$$\sum_{i=1}^{3}\int_0^{L_i} m_i\varphi_{ir}(x_i)\varphi_{is}(x_i)dx_i + M_t\varphi_{3r}(L)\varphi_{3s}(L) + J_t\frac{d\varphi_{3r}(x_3)}{dx_3}|_{x_3=L}\frac{d\varphi_{3s}(x_3)}{dx_3}|_{x_3=L} = \delta_{rs} \tag{16}$$

With the mode shapes obtained, the transverse displacement can be expressed using a modal expansion as $w_i(x_i,\ t) = \sum\varphi_{ir}(x_i)\eta_r(t)$, where $\eta_r(t)$ represents the modal coordinate corresponding to the rth mode. Substituting this expression into Eqs. (1), (3) and (5), and retaining only the fundamental mode ($r = 1$), the system can be reformulated in terms of the modal coordinate as

$$\begin{cases} \ddot{\eta}(t) + 2\zeta\omega\dot{\eta}(t) + \dfrac{1}{2}C_d\rho_a HDU\varphi_3^2(L)\dot{\eta}(t) + \omega^2\eta(t) + \chi V(t) = f_{viv}(t) + f_{flutter}(t) \\ \chi = \theta_p\displaystyle\int_{L_1}^{L_2}\varphi''(x)dx = \theta_p[\varphi'(L_2) - \varphi'(L_1)] \\ f_{viv}(t) = \dfrac{1}{4}\varphi_3(L)C_{l0}\rho_a HDU^2 q(t) \\ f_{flutter}(t) = A_f\sin\left(2\pi f_f t\right)\displaystyle\sum_{j=1}^{n+1}\varphi\left[x - P_f + \frac{W_f}{2} + \frac{W_f}{n}\left(j-1\right)\right] \end{cases} \tag{17}$$

$$\ddot{q}(t) + \varepsilon\omega_f\left[q^2(t) - 1\right]\dot{q}(t) + {\omega_f}^2 q(t) = \varphi_3^2(L)\ddot{\eta}(t) \tag{18}$$

$$I_p(t) + C_pV_p(t) + \chi\dot{\eta}(t) = 0 \tag{19}$$

Finally, the vortex-flutter coupling system can be reformulated into the form of spatial state equations and solved.

2.3. Parametric analysis

To validate the segmented beam dynamics (Eqs. (6)-(16)), we compare the predicted natural frequencies with results obtained from finite element analysis (FEA). Fig. 2b illustrates the first mode shape of the beam segmented into three sections, while Fig. 2c presents the natural frequencies as a function of beam length, showing strong agreement with FEA predictions. Building on this validated beam segment dynamics, we proceed to investigate the vortex-flutter coupling behavior under varying parameter conditions.

Eqs. (17)-(19) govern the complete vortex–flutter coupled system, incorporating multiple physical effects, including the wake oscillator dynamics described in Eq. (3) and the piezoelectric coupling presented in Eq. (5). In solving the coupled system, the mode shapes of the beam are firstly obtained using the segmented beam dynamics (Eqs. (6)-(16)). These mode shapes are then applied to solve the spatial state equations in the modal coordinates derived from Eqs. (17)-(19), resulting in the calculated tip displacement and voltage response of the VFC-WEH. Fig. 2d-2g present the corresponding tip displacement and voltage output under varying flutter frequencies, wind speeds, flag positions, and flag widths, with the amplitude of flutter force as another variable.

VIV is a self-excited oscillation that arises when the vortex shedding frequency approaches the structural natural frequency; thus, its excitation frequency is typically close to the structural natural frequency. Fig. 2d demonstrates that the internal resonance is most pronounced when the flutter frequency closely matches the natural frequency, resulting in increased oscillation amplitude and root-mean-square (RMS) voltage output. When the flutter frequency deviates from VIV frequency, the system undergoes distinct coupling transitions depending on the flutter force amplitude (Supplementary Fig. S1 and S2). At weak

flutter forces, both VIV and flutter coexist, resulting in dual-frequency vibrations (Supplementary Fig. S2b). As the flutter force exceeds a critical threshold, flutter dominates the system response, and the system transitions into a fully forced vibration regime (Supplementary Fig. S2c and S2d).

We further investigate the influence of wind speed on the internal resonance. As shown in Fig. 2e, the optimal coupled oscillation amplitude and RMS voltage are achieved at 4.2 m/s, because of the most intense VIV response at this wind speed. Fig. 2f reveals that increasing the normalized flag position P_u=P_f/L enhances the coupling strength by amplifying the effective torque at the beam tip. The normalized flag width W_u=W_f/L also plays a crucial role, as it determines the force area and total applied flutter force. To maximize the torque without interfering with the bluff body, P_u is correspondingly adjusted to its upper bound during the variation of W_u. When W_u < 0.215, increasing the flag width significantly boosts the coupling strength due to a greater flutter

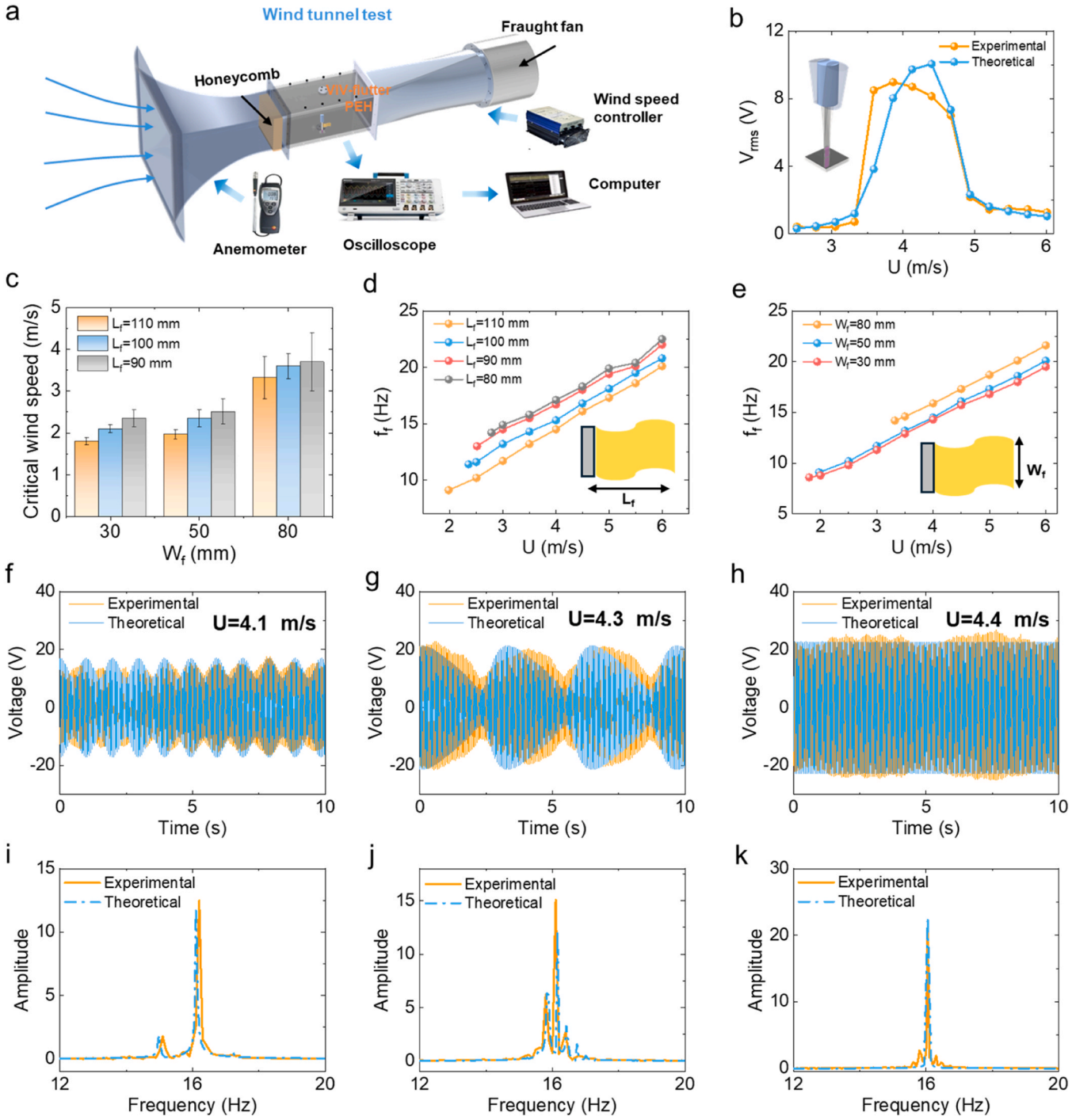

Fig. 3. Experimental validation of the theoretical model. (a) Wind tunnel test setup. The wind tunnel provides a maximum wind speed of 15 m/s. An anemometer is employed to calibrate the wind speed, while an oscilloscope records the electrical output of the VFC-WEH, with data processed via a connected computer. (b) Comparison of VFC-WEH voltage responses between experimental results and theoretical predictions. (c) Critical wind speed of flag flutter as a function of flag length and width. (d) Flutter frequency as a function of flag width and wind speed, with a constant flag length of 110 mm. (e) Flutter frequency as a function of flag length and wind speed, with a constant flag width of 50 mm. (f), (g), (h) Comparison of time-domain voltage responses between experimental results and theoretical predictions at 4.1 m/s, 4.3 m/s and 4.4 m/s. (i), (j), (k) Corresponding frequency-domain voltage responses at 4.1 m/s, 4.3 m/s and 4.4 m/s.

force. However, beyond this threshold, further width increases yield minimal benefit, as the center of the flag shifts farther from the beam tip, resulting in negligible additional torque (Fig. 2g). Additionally, the effect of the flutter force phase angle on harvester performance is examined. Under both dual-frequency and internal resonance conditions, the phase angle has minimal impact on the RMS voltage output of the VFC-WEH (Supplementary Fig. S3a and S3c). Similarly, time-domain voltage waveforms show negligible changes in amplitude, with only corresponding shifts in voltage phase (Supplementary Fig. S3b and S3d). These numerical results provide important insights into the design and optimization of vortex-flutter internal resonance.

2.4. Experimental validation

To guarantee the reliability of our theoretical analysis, the developed VIV model is validated through wind tunnel experiments (Fig. 3a). As illustrated in Fig. 3b and Supplementary Fig. S4a, the predicted responses agree well with the experimental measurements, especially in terms of the wind speed bandwidth where VIV occurs. Minor differences in amplitude are primarily attributed to simplifications in modeling the vortex shedding behavior and the idealization of the wind source. Furthermore, the theoretical VIV frequency closely matches the experimental results (Supplementary Fig. S4b), establishing a solid foundation for accurately capturing the vortex-flutter coupling behavior.

To investigate the flutter dynamics of the flag, related tests are conducted as shown in Supplementary Fig. S5a. The time- and frequency-domain responses confirm the presence of a dominant frequency component, supporting the model assumption that flutter excitations are approximated as a single-frequency periodic excitation (Supplementary Fig. S5b and S5c). Fig. 3c presents the critical flutter wind speed as a function of flag length (90–110 mm) and width (30–80 mm). The results indicate that increasing the flag length or decreasing its width enhances flexibility, thereby lowering the critical flutter wind speed. This is an essential for achieving vortex-flutter internal resonance under low wind conditions. Fig. 3d and Fig. 3e further demonstrate that the flutter frequency rises approximately linearly with wind speed, emphasizing the need to carefully tailor flag geometry so that the flutter frequency falls within the VIV bandwidth and matches the structural natural frequency. Specifically, longer flags lower the flutter frequency, while wider flags raise it. These findings provide practical guidelines for optimizing flag geometry in vortex-flutter coupled systems.

To validate the model's ability to predict vortex-flutter coupling

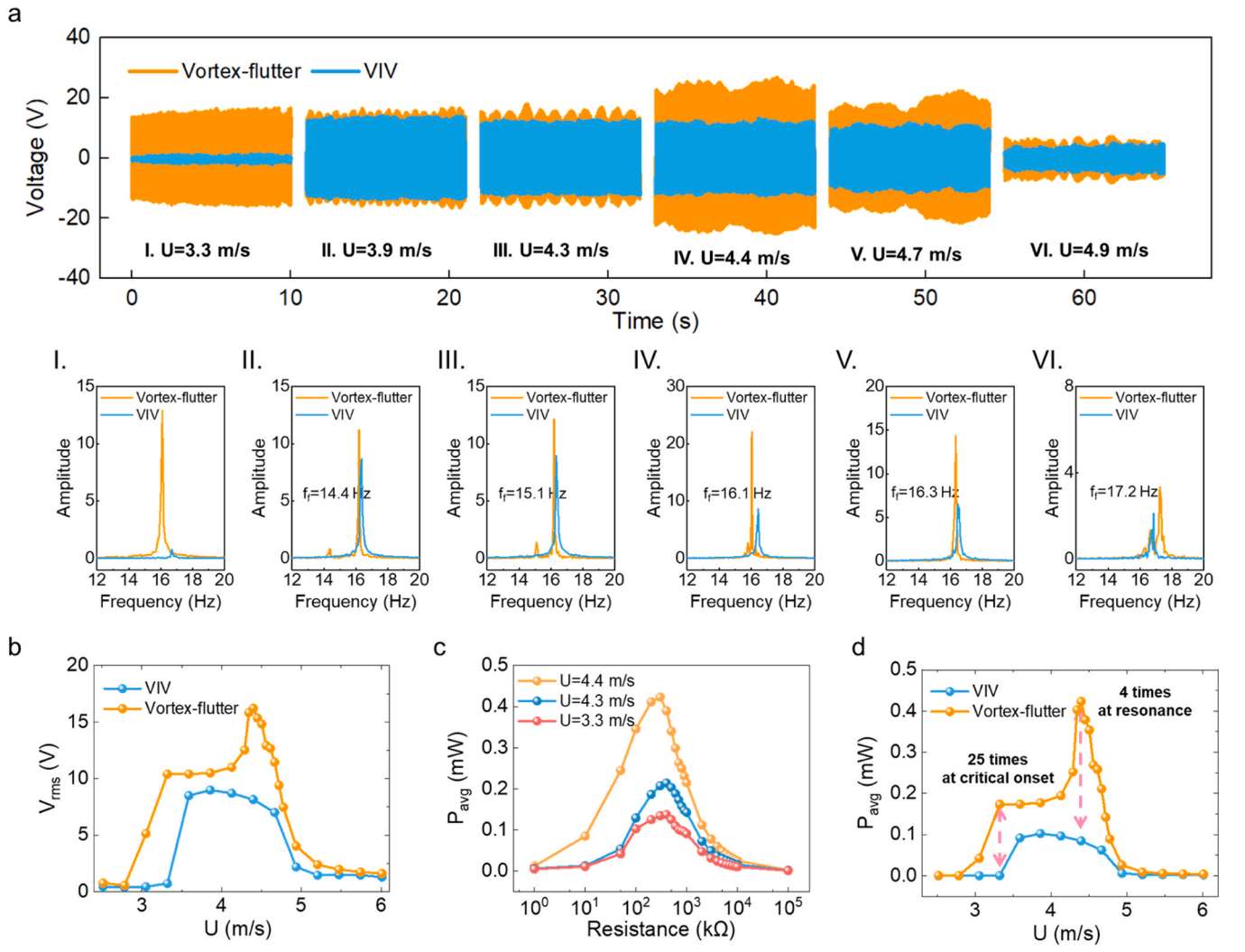

Fig. 4. Performance enhancement under vortex-flutter coupling. (a) Time-domain and frequency-domain voltage waveforms of the harvester under vortex-flutter coupling compared to standalone VIV excitation. (b) RMS voltage of the harvesters as a function of wind speed under vortex-flutter coupling and standalone VIV operation. (c) Average power output of the VFC-WEH versus load resistance. (d) Average output power versus wind speed under both vortex-flutter coupling and standalone VIV operation with an external resistance of 300 kΩ. The flag length and width are 110 and 50 mm.

behavior, experimentally measured flutter frequencies are input into the model, and the flutter excitation amplitude is adjusted to match the voltage responses observed in experiments. Three representative cases with different coupling strengths are selected for comparison (Fig. 3f-3k). When the flutter frequency significantly deviates from the VIV frequency, interference between VIV and flutter leads to amplitude modulation in the voltage response, with a beat frequency of $f_{viv} - f_{flutter}$ (Fig. 3f and 3i). As the flutter frequency approaches the VIV frequency, the beat frequency decreases and the amplitude modulation becomes less pronounced (Fig. 3g and 3j). When the two frequencies coincide, strong vortex-flutter internal resonance occurs, leading to a substantial increase in RMS voltage (Fig. 3h and 3k). These results confirm the model's accuracy in capturing the dynamic behavior of vortex-flutter coupling and further validate the theoretical analyses presented in the previous section.

2.5. Performance benefits of vortex-flutter coupling

Vortex-flutter coupling effectively amplifies vibration intensity, offering notable benefits for enhancing the electrical outputs of WEHs. As illustrated in Fig. 4a, the coupling mechanism increases the output voltage across a range of wind speeds. At 3.3 m/s, an early onset of VIV is triggered due to flutter-induced aerodynamic instability. However, the frequency-domain analysis at this stage indicates a minimal contribution from the flutter force, suggesting that the system is primarily dominated by VIV (Fig. 4a-I). As wind speed increases, the flutter frequency rises accordingly, and amplitude modulation emerges in the time-domain voltage response, characterized by a beat frequency arising from vortex-flutter interaction (Fig. 4a-II and III). In this regime, VIV remains the primary excitation mechanism. When the flutter frequency approaches the VIV frequency, strong coupling occurs, triggering an internal resonance. Due to the wind-speed-dependent nature of flutter frequency, the resonance frequency shifts dynamically (Fig. 4a-IV and V). At 4.9 m/s, the flutter frequency reaches 17.2 Hz, and the system re-enters a dual-excitation regime. However, at this stage, the increased strength of the flutter force allows it to dominate the system's dynamic response (Fig. 4a-VI).

Fig. 4b presents the RMS voltage output of the VFC-WEH across varying wind speeds, highlighting the enhanced electrical performance achieved through vortex-flutter coupling. A visual demonstration of the vortex-flutter internal resonance and its corresponding voltage output at 4.4 m/s is provided in Supplementary Movie S1. To further optimize performance, the optimal load resistance of the VFC-WEH is evaluated at different wind speeds. At 3.3 m/s and 4.3 m/s, the optimal load resistance is found to be 400 kΩ, while at 4.4 m/s, it slightly decreases to 300 kΩ (Fig. 4c), consistent with the optimal impedance of the VIV-based WEH at the same wind speed (Supplementary Fig. S6). To comprehensively evaluate the energy harvesting performance of the VFC-WEH, electrical outputs including RMS voltage, RMS current and average power of the VFC-WEH at the optimal operational wind speed of 4.4 m/s are supplemented in Supplementary Fig. S7**.** Additionally, a direct comparison of average power output between the VFC-WEH and the VIV-based WEH, both under a fixed load resistance of 300 kΩ, is conducted as a function of wind speed (Fig. 4d). At the critical onset, flutter-induced aerodynamic instability results in a 25-fold increase in power output, while at the resonant wind speed of 4.4 m/s, the VFC-WEH delivers a fourfold increase in power output compared to the VIV-based WEH, underscoring the substantial performance enhancement enabled by vortex-flutter coupling.

2.6. Internal resonance under different flutter configurations

While Section 2.3 presents a theoretical analysis of various parameter influences on vortex-flutter coupling, in practice, both flutter frequency and force are inherently dependent on wind speed. Therefore, further experimental investigation is necessary to assess the effects of different flutter configurations on the coupling strength. Among the design variables, flag position is the most flexible and easily adjustable parameter, making it a natural starting point for evaluation. As shown in Fig. 5a and 5d, raising the flag position P_f enhances the equivalent torque applied to the beam, which aligns with theoretical predictions. This increased torque strengthens vortex-flutter coupling, resulting in a higher voltage output. Conversely, when P_f is reduced, the optimal resonant wind speed shifts to a higher value (Fig. 5g). This shift occurs because, at lower wind speeds, the torque generated becomes insufficient to trigger strong coupling, requiring higher wind speeds to provide the necessary excitation. However, as wind speed increases beyond a certain point, the VIV response gradually weakens, leading to a corresponding decrease in electrical output.

When varying the flag length L_f, optimal electrical performance is achieved at a length of 100 mm (Fig. 5b and 5e). For shorter flags $L_f \leq 90$ mm, the output voltage of the VFC-WEH decreases with increasing wind speed after the onset. This reduction is likely due to aerodynamic interference between the flag and the bluff body, as the flag's trailing edge is positioned too close to the wake region of bluff body. However, as the system approaches the internal resonance condition, the yielded voltage increases sharply. As illustrated in Fig. 5h, the resonant wind speed decreases with shorter flag lengths, since these configurations reach the required flutter frequency at lower flow velocities. The highest voltage at the internal resonance is achieved when $L_f = 100$ mm, representing an optimal balance between the intensities of VIV and flutter excitations.

The effect of flag width W_f on vortex-flutter coupling is also investigated. During this analysis, the flag position P_f is set to its maximum allowable value to maximize the generated flutter torque. As shown in Fig. 5c and 5f, the narrowest flag ($W_f = 30$ mm) yields the highest overall electrical output within the VIV operational bandwidth. This performance is attributed to the relatively stable flutter frequency of narrow flags across a wide range of wind speeds, facilitating consistent vortex-flutter coupling. Interestingly, the resonant wind speed achieves the maximum value when $W_f = 50$ mm (Fig. 5i), reflecting the combined effects of flag width and position on the system's dynamic behavior. However, the optimal resonant voltage output is yielded at $W_f = 30$ mm. As previously analyzed, increasing the flag width does not necessarily improve coupling performance. Although wider flags produce greater overall flutter force, their center shifts farther from the beam tip, reducing the effective torque generated. Moreover, wider flags, such as $W_f = 70$ mm, are more likely to undergo aerodynamic interference with the bluff body, further weakening coupling efficiency. These findings highlight the trade-off between maximizing equivalent torque and maintaining efficient internal resonance, underscoring the importance of optimizing flutter configuration to achieve optimal energy harvesting performance.

2.7. Application demonstrations of VFC-WEH

Given its enhanced performance, the VEH-WEH holds promise for broader self-powered applications. As illustrated in Fig. 6a, the harvester is capable of powering a set of LEDs, showcasing its feasibility for low-power lighting applications. Additionally, capacitor charging experiments are conducted using a full-wave bridge rectifier circuit (Fig. 6c). When charging a 47 μF capacitor, the charging rate is found to be highly dependent on the vortex-flutter coupling strength, with the fastest rate observed at a resonant wind speed of 4.4 m/s (Fig. 6d). Furthermore, Fig. 6e illustrates the capacitor charging performance at 4.4 m/s across various capacitance values, demonstrating the capability of the VFC-WEH to serve as a reliable power source for low-power electronics.

Finally, a self-sufficient wireless temperature monitoring system is successfully implemented using the VFC-WEH (Fig. 6b). In this system, the VFC-WEH harvests ambient wind energy and converts it into electrical power, while the integrated WSN handles energy management, storage, and signal transmission. The measured temperature is displayed

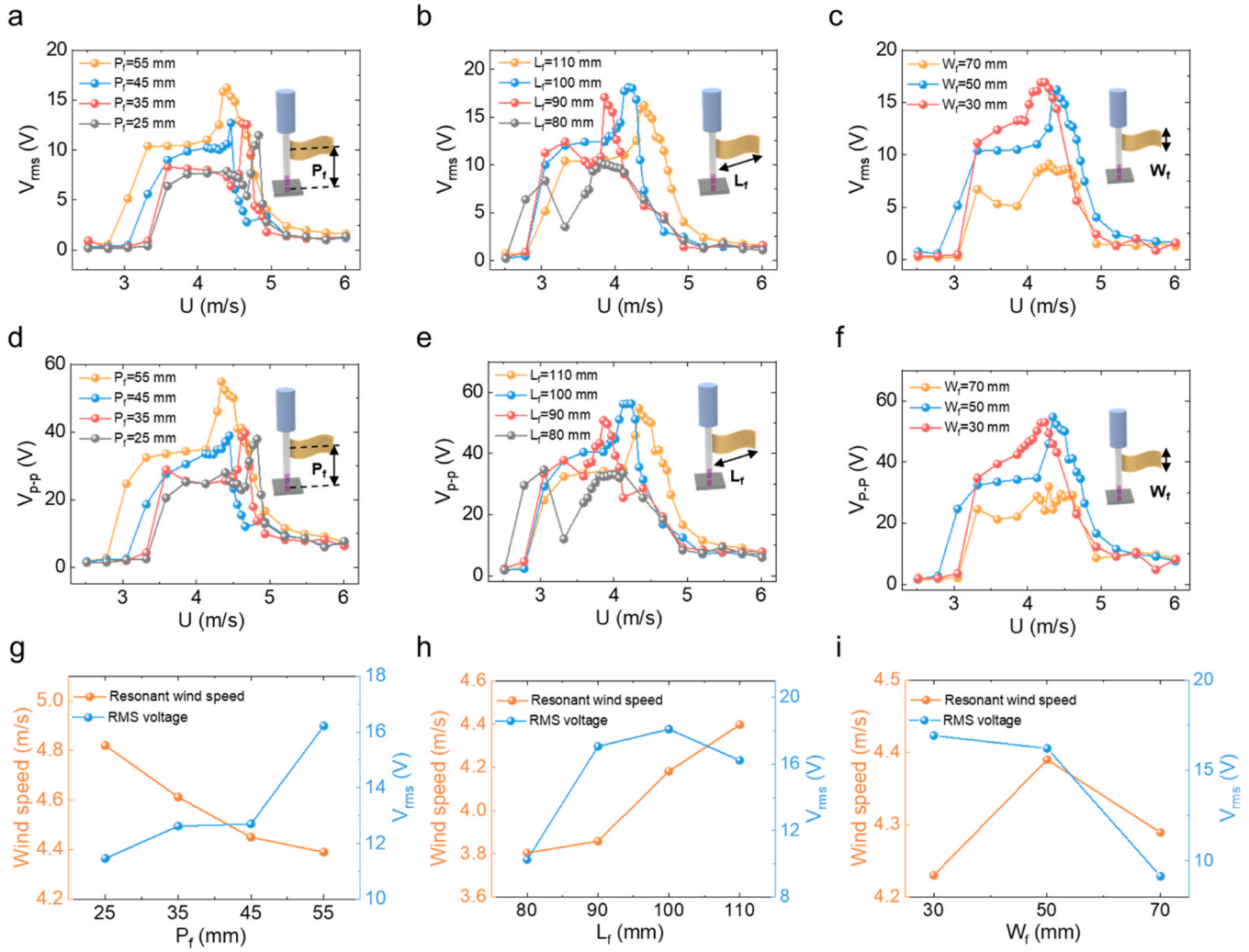

Fig. 5. Vortex-flutter coupling under different flutter configurations. (a), (b), (c) RMS voltage of the VFC-WEH versus wind speed for varying flag position (25–55 mm), flag length (80–110 mm), and flag width (30–70 mm). (d), (e), (f) Peak-to-peak voltage versus wind speed for the same flag position, length, and width configurations. (g), (h), (i) Resonant wind speed and corresponding electrical output under different flag position, length, and width conditions.

in real time via a custom-designed mobile application. As illustrated in Fig. 6f and Supplementary Fig. S8, the WSN consists of an energy management module and a signal transmission module. The AC output generated by the VFC-WEH is first rectified into DC voltage using a full-bridge rectifier. This voltage is then buffered and stabilized by a capacitor in the energy management module. A buck converter, based on the LTC3588–1 chip, regulates power delivery. The converter features an energy-aware control mechanism with an undervoltage lockout (UVLO) function, configured through circuit settings to prevent operation under inefficient voltage levels. This ensures stable system performance and maximizes energy conversion efficiency. The regulated DC voltage powers the signal transmission module, which comprises a microcontroller unit (MCU), a temperature sensor, and a wireless transceiver.

Fig. 6g compares the instantaneous operational voltage of the WSN when powered by the VFC-WEH versus a conventional VIV-based WEH. A voltage rise to 5 V, followed by a sharp drop, indicates successful activation of the signal transmission module. The vortex-flutter internal resonance significantly reduces the start-up time from 44 to 20 s and shortens the signal transmission interval from 19.6 to 8.3 s. As summarized in Fig. 6h and Supplementary Fig. S9, the system maintains stable and reliable power delivery across varying wind speeds, highlighting the VFC-WEH's strong potential for enabling self-powered operation in real-world, variable wind environments.

3. Conclusion

In this paper, we report the first observation of a vortex-flutter internal resonance phenomenon and its application for wind energy harvesting. This work encompasses theoretical modeling, numerical simulation, and experimental validation of a VFC-WEH. By introducing flutter excitations into a conventional VIV-based WEH, we uncover a previously unexploited internal resonance mechanism that significantly enhances energy conversion performance.

The aerodynamic model developed in this work incorporates beam segment dynamics, piezoelectric coupling, and VIV and flutter excitations to elucidate the vortex-flutter coupled mechanism. While the current model does not account for nonlinear interactions introduced by flutter within the fluid–structure system, it successfully captures the key physical behaviors, as confirmed through experimental validation. Future modeling efforts could benefit from incorporating advanced fluid-structure interaction methods or high-fidelity computational fluid dynamics simulations to more accurately resolve unsteady flow phenomena and flutter-induced turbulence.

Compared to conventional VIV-based WEHs, the VFC-WEH exhibits a 25-fold and fourfold increases in output power at critical onset and internal resonance, along with substantial reductions in startup time and signal transmission intervals when powering a WSN. These improvements are attributed to the synergistic interaction between VIV and

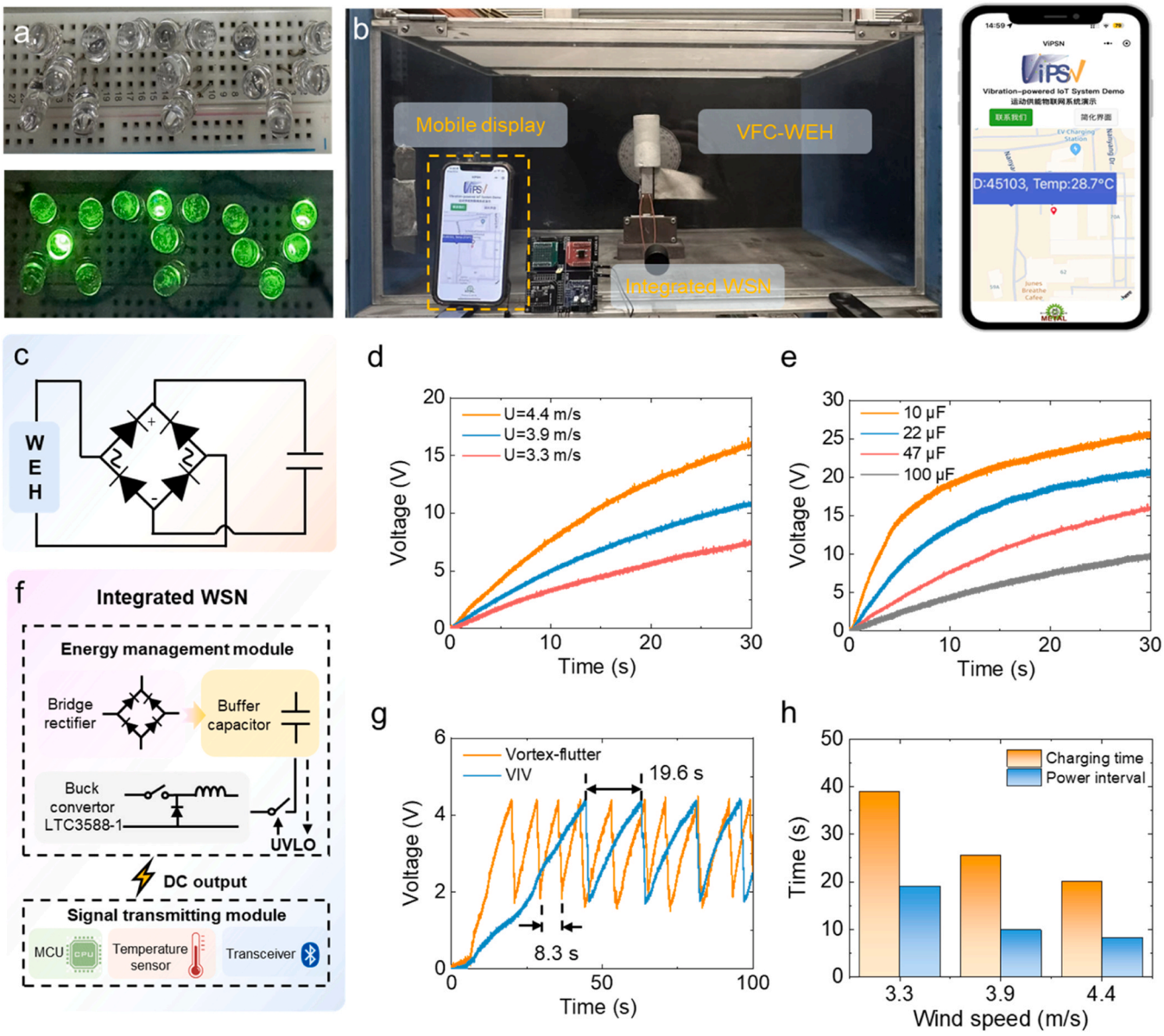

Fig. 6. Application demonstrations of the VFC-WEH. (a) Lighting LEDs using the VFC-WEH. (b) Photograph of a self-sufficient wireless temperature monitoring system enabled by the VFC-WEH. (c) Circuit configuration for capacitor charging. (d) Capacitor charging performance at different wind speeds using a 47 μF capacitor. (e) Comparison of capacitor charging performance with different capacitance values at 4.4 m/s. (f) Circuit principle of the integrated WSN. (g) Comparison of the operational voltage of the WSN powered by the VFC-WEH and a conventional VIV-based WEH at 4.4 m/s. (h) Power supply performance of the VFC-WEH at different wind speeds.

flutter, which facilitates more efficient energy conversion at low wind speeds. Importantly, the coupling behavior is readily tunable by adjusting parameters such as flag position, length, and width, offering a flexible design for diverse deployment scenarios.

Although currently optimized for low-power applications such as environmental monitoring and distributed IoT nodes, the VFC-WEH represents a critical step toward scalable, self-powered infrastructure. The VFC-WEH employs an off-the-shelf MFC and consists entirely of low-cost, sustainable, and easy-to-fabricate components, allowing for cost-effective and environmentally friendly implementation. By leveraging multi-mode FIV coupling, future designs are expected to sustain high performance across a broad wind speed spectrum. Moreover, combining the VFC-WEH with advanced power management techniques, such as synchronized charge extraction and adaptive impedance matching, could further improve the conversion efficiency.

Within the broader landscape of sustainable energy technologies, the VFC-WEH contributes to the advancement of low-cost, decentralized energy harvesting solutions. As global efforts toward carbon neutrality accelerate, particularly in off-grid and underserved regions, miniature and high-performance WEHs like the VFC-WEH will play an increasingly important role. With its simple construction, tunable design, and demonstrated functionality, this work offers a promising foundation for the next generation of resilient, green energy systems.

4. Methods

4.1. Theoretical modeling and numerical simulations of VFC-WEH

In the theoretical modeling, the beam is segmented into three sections to account for the partial coverage of the MFC on the host beam. The beam segment dynamics model is validated through finite element simulations using COMSOL Multiphysics 6.3. The space state equations

of the aero-electro-mechanical model for the VFC-WEH are implemented in MATLAB R2024a and numerically solved using the ode45 solver. The parameters for modeling are provided in Supplementary Table. S1.

4.2. Fabrication of VFC-WEH

The VFC-WEH is composed of an off-the-shelf MFC sheet, a cylindrical bluff body, an aluminum host beam and a flexible flag. The foam bluff body features a dimeter of 40 mm and a height of 80 mm. The aluminum beam measures 120 mm in length, 17 mm in width, and 0.6 mm in thickness. The MFC (M2814-P2), with dimensions of $28 \times 14 \times 0.3$ mm^3, is attached on the fixed end of the host beam using an epoxy resin adhesive. The flag is fabricated from a nickel-coated textile and has dimensions of $110 \times 0.1 \times 50$ mm^3 (length $\times$ thickness $\times$ height). The center of the flag is positioned 55 mm from the base of the harvester.

4.3. Wind tunnel tests and electrical measurement

Fluid-related experiments are conducted in a wind tunnel (EdLab-QUIP FM670) at the CEE Protective Engineering Laboratory, Nanyang Technological University. The tunnel features a cross-sectional area of 300×300 mm^2 and a maximum wind velocity of 15 m/s. Wind speed is calibrated using an anemometer (TESTO 425). For flag displacement measurements, the flag is mounted on a rigid support beam using a fixture, with a reflective sticker attached near its fixed end. Displacements are measured using a laser sensor (Keyence LK-H157), with output signals recorded through a data acquisition module (NI 9229).

Electrical measurements of the VFC-WEH and the conventional VIV-based WEH are performed using a four-channel oscilloscope (Tektronix MSO44) to record the generated output voltage signals. For resistance optimization and capacitor charging experiments, a tunable resistance substitute (IET RS-200W) and a capacitance substitute (IET RCS-500) are employed to simulate various electrical load conditions.

4.4. Implementation of the integrated WSN

The printed circuit board of the integrated WSN for mobile temperature monitoring is designed using Altium Designer 20, while the embedded algorithm is implemented in in Keil μVision5. The Buck convertor in the energy management module is realized with the LT3588–1 controller chip, providing voltage regulation with an energy conversion efficiency ranging from 80 % to 90 %. The signal transmission module is built around the nRF52832 Bluetooth system-on-chip. Temperature data are wirelessly transmitted and received by a mobile device through a custom software interface embedded within the WeChat platform.

CRediT authorship contribution statement

Chengjia Han: Formal analysis, Data curation. **Xin Li:** Validation, Software, Resources. **Chaoyang Zhao:** Visualization, Supervision. **Liwei Dong:** Writing – review & editing, Writing – original draft, Validation, Methodology, Data curation, Conceptualization. **Qian Tang:** Writing – original draft, Visualization, Methodology, Formal analysis. **Yaowen Yang:** Writing – review & editing, Supervision, Project administration, Funding acquisition, Formal analysis, Conceptualization. **Guobiao Hu:** Methodology, Investigation. **Fan Yang:** Writing – review & editing, Visualization, Validation, Project administration, Funding acquisition.

Declaration of Competing Interest

The authors declare that they have no known competing financial interests or personal relationships that could have appeared to influence the work reported in this paper.

Acknowledgments

This research is sponsored by the NTU grant 020671-00001, the National Natural Science Foundation of China (Grant No. 12202276), Fundamental Research Funds for the Central Universities (Grant No. YG2025ZD18), Shanghai Municipal Health Commission (Grant No. 2024ZZ2002), and Innovative research team of high-level local universities in Shanghai.

Appendix A. Supporting information

Supplementary data associated with this article can be found in the online version at doi:10.1016/j.nanoen.2025.111339.

Data availability

Data will be made available on request.

References

[1] M.A.M. Hasan, W. Zhu, C.R. Bowen, Z.L. Wang, Y. Yang, Triboelectric nanogenerators for wind energy harvesting, Nat. Rev. Electr. Eng. 1 (2024) 453–465.
[2] F.-R. Fan, Z.-Q. Tian, Z. Lin Wang, Flexible triboelectric generator, Nano Energy 1 (2012) 328–334.
[3] L. Long, W. Liu, Z. Wang, W. He, G. Li, Q. Tang, H. Guo, X. Pu, Y. Liu, C. Hu, High performance floating self-excited sliding triboelectric nanogenerator for micro mechanical energy harvesting, Nat. Commun. 12 (2021) 4689.
[4] L. Dong, G. Hu, Q. Tang, C. Zhao, F. Yang, Y. Yang, Advanced aerodynamics-driven energy harvesting leveraging galloping-flutter synergy, Adv. Funct. Mater. 35 (2025) 2414324.
[5] J. Wang, S. Zhou, Z. Zhang, D. Yurchenko, High-performance piezoelectric wind energy harvester with Y-shaped attachments, Energy Convers. Manag. 181 (2019) 645–652.
[6] J. Hu, S. Liu, Y. Huo, B. Yang, Y. Yin, M.-L. Tan, P. Liu, K. Cai, W. Ji, Piezoelectric vitamin-based self-assemblies for energy generation, Adv. Mater. 37 (2025) 2417409.
[7] X. Zhao, A. Nashalian, I.W. Ock, S. Popoli, J. Xu, J. Yin, T. Tat, A. Libanori, G. Chen, Y. Zhou, J. Chen, A soft magnetoelastic generator for wind-energy harvesting, Adv. Mater. 34 (2022) 2204238.
[8] M. Zhu, Y. Yu, J. Zhu, J. Zhang, Q. Gao, H. Li, Y. Zhang, Z.L. Wang, T. Cheng, Bionic blade lift-drag combination triboelectric-electromagnetic hybrid generator with enhanced aerodynamic performance for wind energy harvesting, Adv. Energy Mater. 13 (2023) 2303119.
[9] L. Dong, J. Zuo, Vibration-adaptive energy management technology for self-sufficient wireless ECP braking systems on heavy-haul trains, Mech. Syst. Signal Process. 223 (2025) 111940.
[10] K. Calautit, C. Johnstone, State-of-the-art review of micro to small-scale wind energy harvesting technologies for building integration, Energy Convers. Manag. X 20 (2023) 100457.
[11] X. Li, L. Teng, H. Tang, J. Chen, H. Wang, Y. Liu, M. Fu, J. Liang, ViPSN: a vibration-powered IoT platform, IEEE Internet Things J. 8 (2021) 1728–1739.
[12] L. Dong, G. Hu, Y. Zhang, W. Ding, S. Qu, Q. Tang, C. Zhao, Y. Yang, F. Yang, Metasurface-enhanced multifunctional flag nanogenerator for efficient wind energy harvesting and environmental sensing, Nano Energy 124 (2024) 109508.
[13] Y. Li, H. Deng, H. Wu, Y. Luo, Y. Deng, H. Yuan, Z. Cui, J. Tang, J. Xiong, X. Zhang, S. Xiao, Rotary wind-driven triboelectric nanogenerator for self-powered airflow temperature monitoring of industrial equipment, Adv. Sci. 11 (2024) 2307382.
[14] H.-X. Zou, L.-C. Zhao, Q. Wang, Q.-H. Gao, G. Yan, K.-X. Wei, W.-M. Zhang, A self-regulation strategy for triboelectric nanogenerator and self-powered wind-speed sensor, Nano Energy 95 (2022) 106990.
[15] X. Li, Q. Gao, Y. Cao, Y. Yang, S. Liu, Z.L. Wang, T. Cheng, Optimization strategy of wind energy harvesting via triboelectric-electromagnetic flexible cooperation, Appl. Energy 307 (2022) 118311.
[16] C. Zhang, X. Yang, B. Zhang, K. Fan, Z. Liu, Z. Liu, The efficient energy collection of an autoregulatory driving arm harvester in a breeze environment, Micromachines 14 (2023) 2032.
[17] X.Q. Wang, R.M.C. So, Y. Liu, Flow-induced vibration of an Euler-Bernoulli beam, J. Sound Vib. 243 (2001) 241–268.
[18] L. Ma, K. Lin, D. Fan, J. Wang, M.S. Triantafyllou, Flexible cylinder flow-induced vibration, Phys. Fluids 34 (2022) 011302.
[19] L. Dong, Q. Tang, C. Zhao, G. Hu, S. Qu, Z. Liu, Y. Yang, Flag-type hybrid nanogenerator utilizing flapping wakes for consistent high performance over an ultra-broad wind speed range, Nano Energy 119 (2024) 109057.
[20] A. Duranay, A.E. Demirhan, E. Dobrucali, O.K. Kinaci, A review on vortex-induced vibrations in confined flows, Ocean Eng. 285 (2023) 115309.

[21] Z. Li, J. Zhang, H. Xu, S. Zhou, L. Cheng, Chaotic responses across the potential barrier of bistable vortex-induced vibration energy harvesters, Physica D Nonlinear Phenomena 470 (2024) 134374.
[22] L. Dong, C. Zhao, S. Qu, W. Ding, G. Hu, C. Han, Y. Yang, Structural galloping suppression with high-frequency flutter, Int. J. Mech. Sci. 287 (2025) 109928.
[23] Z. Li, S. Zhou, Z. Yang, Recent progress on flutter-based wind energy harvesting, Int. J. Mech. Syst. Dyn. 2 (2022) 82–98.
[24] Z. Li, W. Lyu, C. Gong, S. Zhou, L. Cheng, Experimental investigation and dynamic analysis of a novel electromagnetic energy harvester based on airfoil flutter, Energy Convers. Manag. 326 (2025) 119471.
[25] C. Zhang, G. Hu, D. Yurchenko, P. Lin, S. Gu, D. Song, H. Peng, J. Wang, Machine learning based prediction of piezoelectric energy harvesting from wake galloping, Mech. Syst. Signal Process. 160 (2021) 107876.
[26] X. Fan, K. Guo, Y. Wang, Toward a high performance and strong resilience wind energy harvester assembly utilizing flow-induced vibration: Role of hysteresis, Energy 251 (2022) 123921.
[27] L. Zhao, L. Tang, Y. Yang, Enhanced piezoelectric galloping energy harvesting using 2 degree-of-freedom cut-out cantilever with magnetic interaction, Jpn. J. Appl. Phys. 53 (2014) 060302.
[28] S. Zhou, J. Wang, Dual serial vortex-induced energy harvesting system for enhanced energy harvesting, AIP Adv. 8 (2018) 075221.
[29] K. Yang, J. Wang, D. Yurchenko, A double-beam piezo-magneto-elastic wind energy harvester for improving the galloping-based energy harvesting, Appl. Phys. Lett. 115 (2019) 193901.
[30] R. Naseer, H.L. Dai, A. Abdelkefi, L. Wang, Piezomagnetoelastic energy harvesting from vortex-induced vibrations using monostable characteristics, Appl. Energy 203 (2017) 142–153.
[31] L.B. Zhang, A. Abdelkefi, H.L. Dai, R. Naseer, L. Wang, Design and experimental analysis of broadband energy harvesting from vortex-induced vibrations, J. Sound Vib. 408 (2017) 210–219.
[32] K. Li, Z. Yang, S. Zhou, Performance enhancement for a magnetic-coupled bi-stable flutter-based energy harvester, Smart Mater. Struct. 29 (2020) 085045.
[33] L. Zhao, Y. Yang, An impact-based broadband aeroelastic energy harvester for concurrent wind and base vibration energy harvesting, Appl. Energy 212 (2018) 233–243.
[34] J. Pan, X. Zhang, Y. Cheng, J. Zhang, W. Qin, Harvesting both wind energy and vibration energy by a zigzag structure with hybrid magnetic and piezoelectric effects, Mech. Syst. Signal Process. 224 (2025) 112066.
[35] H.L. Dai, A. Abdelkefi, L. Wang, Piezoelectric energy harvesting from concurrent vortex-induced vibrations and base excitations, Nonlinear Dyn. 77 (2014) 967–981.
[36] K. Yang, T. Qiu, J. Wang, L. Tang, Magnet-induced monostable nonlinearity for improving the VIV-galloping-coupled wind energy harvesting using combined cross-sectioned bluff body, Smart Mater. Struct. 29 (2020) 07LT01.
[37] J. Wang, B. Xia, D. Yurchenko, H. Tian, Enhanced performance of cutting angle cylinder piezoelectric energy harvester via coupling vortex-induced vibration and galloping, Mech. Syst. Signal Process. 205 (2023) 110838.
[38] X. Shan, H. Tian, H. Cao, T. Xie, Enhancing performance of a piezoelectric energy harvester system for concurrent flutter and vortex-induced vibration, Energies 13 (2020).
[39] A. Kurs, A. Karalis, R. Moffatt, J.D. Joannopoulos, P. Fisher, M. Soljačić, Wireless power transfer via strongly coupled magnetic resonances, Science 317 (2007) 83–86.
[40] J. Zhang, J. Zhang, C. Shu, Z. Fang, Enhanced piezoelectric wind energy harvesting based on a buckled beam, Appl. Phys. Lett. 110 (2017) 183903.
[41] H.T. Li, H. Ren, M.J. Shang, Q. Lv, W.Y. Qin, Dynamics and performance evaluation of a vortex-induced vibration energy harvester with hybrid bluff body, Smart Mater. Struct. 32 (2023) 045016.
[42] S. Fang, H. Du, T. Yan, K. Chen, Z. Li, X. Ma, Z. Lai, S. Zhou, Theoretical and experimental investigation on the advantages of auxetic nonlinear vortex-induced vibration energy harvesting, Appl. Energy 356 (2024) 122395.
[43] J. Wang, L. Luo, D. Yurchenko, G. Hu, Equivalent circuit analysis of a nonlinear vortex-induced vibration piezoelectric energy harvester using synchronized switch technique, IEEE Trans. Ind. Electron. 72 (2025) 4865–4876.
[44] L. Zhao, Y. Yang, Enhanced aeroelastic energy harvesting with a beam stiffener, Smart Mater. Struct. 24 (2015) 032001.
[45] M.L. Facchinetti, E. de Langre, F. Biolley, Coupling of structure and wake oscillators in vortex-induced vibrations, J. Fluids Struct. 19 (2004) 123–140.
[46] L. Zhao, L. Tang, Y. Yang, Comparison of modeling methods and parametric study for a piezoelectric wind energy harvester, Smart Mater. Struct. 22 (2013) 125003.
[47] O.A. Bauchau, J.I. Craig, Euler-Bernoulli beam theory, Springer, 2009.

Liwei Dong obtained his Ph.D. degree from Tongji University in 2024. He currently works as a Research Fellow at Nanyang Technological University. His research interests include wind and mechanical energy harvesting, flexible sensors and interface circuits for energy harvesting.

Qian Tang received his Ph.D. degree in Applied Physics from Chongqing University, China. Now he is working in the School of Physics and New Energy, Chongqing University of Technology, Chongqing, China. His current research interest is triboelectric nanogenerator based self-powered systems.

Xin Li received the master's and Ph.D. degrees in communication and information system from The University of Chinese Academy of Sciences, Beijing, China in 2018 and 2022, respectively. He currently works as an Associate Professor with the Guanzhou Institute of Technology, Xidian University, China. His research interests include battery-free IoT, Intermittent computing and vibration energy harvesting.

Chaoyang Zhao obtained his Ph.D. from Nanyang Technological University (NTU) in 2023. He joined Professor Yang Yaowen's research group in 2018 and currently working as a Research Fellow at NTU. His research interests mainly focus on energy harvesting, nonlinear dynamics, structural health monitoring and composite sensors.

Chengjia Han obtained B.Sc. degrees from Wuhan University of technology, Wuhan, China. He obtained Ph.D. degree from Southeast University, Nanjing, China. He is currently working as a research fellow at Nanyang Technological University. His main research interest is artificial intelligence in civil and transportation engineering.

Guobiao Hu received his B.Eng. degree from Southwest Jiaotong University, China, in 2012, Diplôme d'Ingénieur from École Centrale Paris, France, in 2015, and Ph.D. degree from the University of Auckland, New Zealand, in 2020. He is currently a tenure-track Assistant Professor with the Internet of Things Thrust, Information Hub, the Hong Kong University of Science and Technology (Guangzhou), China. His research interests include vibration & wind energy harvesting and acoustic-elastic metamaterials.

Fan Yang is currently a professor at Shanghai Jiao Tong University, where he has been serving since July 2022. From 2018–2020, he participated in a joint Ph.D. training program at the University of Wisconsin–Madison and received his Ph.D. from Southwest Jiaotong University in 2020. In December 2020, he joined Tongji University as an assistant professor. His research focuses on the synthesis of functional biomaterials, particularly piezoelectric materials, and the development of implantable and wearable devices for medical diagnostics and therapeutic applications.

Yaowen Yang is currently a Professor in the School of Civil and Environmental Engineering, Nanyang Technological University, Singapore. He is an expert researcher in the areas of small energy harvesting and structural and geotechnical monitoring. His research encompasses aeroelastic and vibration energy harvesting, metamaterials, structural health monitoring, and uncertainty analysis in structural dynamics. Prof. Yang has secured substantial research grants from various funding sources and industry partners, resulting in over 330 publications in journals and conferences. Prof Yang received his B.Eng and M.Eng from Shanghai Jiao Tong University and Ph.D from Nanyang Technological University.